

Modelling the Initiation of Dust Eruptions

M.J. McGuinness*, H. Singh

*School of Mathematics, Statistics and Operations Research, Victoria University of Wellington,
New Zealand*

Abstract

We present a new model for the initiation of high-speed eruptive two-phase dust flows in the laboratory. Shock-tube experiments have been conducted on beds of solid particles in nitrogen under high pressure, which are suddenly decompressed. Our model is successful in explaining the slab-like structures that are often observed during initiation of bed movement, by considering the interaction between the compressible flow of gas through the bed and the stress field in the particle bed, which ruptures when bed cohesion is overcome by the effective stress in the bed generated by the gas flow. Our model includes the effects of overburden and wall friction, and predicts that all layered configurations will rupture initially in this fashion, consistent with experimental observation. We also find that the modelled dependence of layer size on particle size is a good match to experiment. The volcanological implication is that the source in Vulcanian and Plinian eruptions is typically heterogeneous in nature.

Keywords: explosive fragmentation, mathematical model, dusty gas flow, shock tube, high speed two-phase flow, layer formation
74H10, 74F10, 74H14

1. Introduction

Explosive volcanic activity is expressed in a wide range of forms, ranging from Hawaiian fire fountaining and Strombolian eruptions to highly energetic Vulcanian and Plinian eruptions. Fragmentation types may be roughly divided into two end-members depending on magma viscosity. In low-viscosity magma, proposed fragmentation mechanisms include bursting bubbles and foam instability

*Phone: +64 4 463 5059; Email: Mark.McGuinness@vuw.ac.nz

(Verhoogen, 1951; Sparks, 1978; Mangan & Cashman, 1996). On the other hand, in high-viscosity magma bubble growth is constrained by viscous forces resulting in over-pressurized vesicles. This magma tends to fragment in a brittle manner when the strength of the magma is exceeded, and this is usually taken to be due to the presence of pressurized vesicles under rapid decompression (McBirney & Murase, 1970; Heiken & Wohletz, 1991; Gilbert & Sparks, 1998; Cashman et al., 2000; Fowler et al., 2009), although high strain rates can also lead to brittle fracture (Papale et al., 1998; Papale, 1999; Dingwell & Webb, 1989). Layer-by-layer fragmentation is now widely accepted as a predominant fracturing process associated with rapid decompression (Cashman et al., 2000; Melnik, 2000; Ichihara et al., 2002; Namiki & Manga, 2005; Scheu et al., 2006, 2008).

Explosive eruptions are characterized by high-velocity flows of mixtures of solid particles and gas. Laboratory experiments with shock-tube apparatus have been conducted in order to better understand fragmentation and flow processes in Vulcanian and Plinian eruptions, and experiments with dusts were originally reported in this journal (Anilkumar et al, 1993). These experiments are relevant to the initiation of high-velocity eruptive flows as well as to the interpretation of deposits. The features we examine particularly in this paper help to inform volcanologists about the inhomogeneity of the material leaving the volcanic vent and acting as a source for an ash plume. In particular, the flows are observed to be strongly inhomogeneous, with high-concentration regions interspersed with low-concentration regions (Anilkumar et al, 1993).

The materials used in these experiments vary from packed beds of spheres of glass and steel (Anilkumar et al, 1993; Anilkumar, 1989), through weakly cohesive artificial porous structures (Mader et al., 1994; Philips et al., 1995; Ichihara et al., 2002; Namiki & Manga, 2005; Kameda et al., 2008), to competent natural samples of volcanic rock (Alidibirov, 1994; Martel et al., 2000; Spieler et al., 2004b; Scheu et al., 2006, 2008). A number of these papers are motivated by a desire to understand and shed light on the development of physical models for the formation of volcanic ash, and acknowledge the importance of this understanding for the intensity and character of explosive eruptions, as well as for the morphology of pyroclasts and grain size distribution.

Shock-tube experiments conducted on samples of natural eruptive competent rock and weakly cohesive materials display a characteristic length-scale for primary fragmentation, so that slabs of solid material of approximately the same thickness successively break off from the remaining stationary material. When the sample is competent, it is necessary to anchor the initial sample into the shock-tube with glue or by having a tight fit, to prevent it from immediately moving up

the tube. Fragmenting sections, then, have simultaneously broken away from the remaining sample, and from the glued or tight-fitting sides.

A novel recent mathematical model of gas flow through porous rock has successfully explained the appearance of this lengthscale for competent rock samples (Fowler et al., 2009; McGuinness et al., 2012). In this modelling, a nonlinear diffusion equation was derived for the movement of gas through the rock sample, driven by the arrival at the sample surface of an expansion wave. The resulting variations in gas pressure stress the rock sample. This stress increases towards critical tensile strength while penetrating deeper into the still stationary sample. When tensile strength is exceeded, this occurs at a local maximum of stress some distance into the sample, causing a slab of material to fragment and move upwards, revealing a new upper surface at which the same process begins again. A key role is played in this previous modelling work by the mechanism that holds the remaining rock in place. Without glue or a tight fit, the model predicts that the maximum stress is at the base of the sample, not partway down, causing the entire sample to lift off, as is observed in practice.

It may come as something of a surprise then, that when packed beds of small spheres with small cohesion are used instead of competent samples in shock-tube experiments, the very first mobilisation event observed is again the formation of horizontal cracks on a certain lengthscale at initiation of movement. The resulting slabs of beads are closely associated with the large-scale heterogeneities in flow density that are the main feature of the complicated flow structure that subsequently develops (Anilkumar et al, 1993; Anilkumar, 1989; Cagnoli et al, 2002).

The tensile strengths of the bead beds considered is less than 100 Pa, compared with a tensile strength of over 1 MPa for rock. The over-pressures involved in the dust experiments are of the order of one bar, compared to about 100 bars for rocks.

The formation of slabs at initiation of movement of bead beds under transient gas pressure changes in shock tubes is not a feature of fluidised beds with gradually increased steady gas through-flow. As noted in Valverde et al (1998), the first fracture of such beds is always at the bottom of the bed. Smaller-scale slab structures in steady fluidised beds are only manifested for some classes of powders as slug flow features at gas flowrates significantly higher than required for fluidisation. Incompressible gas flow is a useful approximation in most modelling of fluidised beds, whereas compressible gas flow is central to the shock-tube setup since gas decompression is the cause of gas flow.

Our aim in this paper is to explain the formation of these slab structures at the onset of mobilisation of a low-cohesion bed of particles under the transient compressible gas flow imposed by the shock-tube setup, by using a modification of the

modelling approach that has been so successful used by Fowler et al. (2009) and McGuinness et al. (2012) for shock-tube experiments on competent rock samples.

We review some details of the dust shock-tube experiments in the next section, then we introduce the mathematical model describing conservation of mass and momentum, and relating stress and strain, in the following section. In that section we derive a reduced set of equations describing gas pressures and stress, after rescaling and setting small parameters to zero. Solutions are presented in the following section, then the rupture condition is considered in the next section, followed by conclusions.

2. Dust Experiments

The experiments prompting this paper are reported by Anilkumar (1989) and Anilkumar et al (1993). A shock tube apparatus is used to fluidize packed beds of spheres sourced from a range of materials and with nitrogen gas as the working fluid, with a range of bed heights from 15–60cm, bed width of 3.8 cm with a square geometry, sphere diameters in the range 125–1000 μm , final speeds of 15–60 m/s, and accelerations in excess of 150g. In that apparatus, the timescale for pressure to drop by a factor of e is about 1 ms. In contrast, Cagnoli et al (2002) use smaller sphere diameters (38 and 95 μm) and smaller pressure drops (200–900 mbar), mobilised by sudden decompression of a dry air environment. In some of Anilkumar’s experiments the bed of spheres rests on a solid base, in others it rests on a mesh with more high-pressure nitrogen below. The test section is pressurized to 2–3 bars gauge (barg, that is, bars above atmospheric pressure), and the pressure is released explosively at the top by rupturing a diaphragm separating the high pressure section from a 7–13m long exhaust region at atmospheric pressure. Windows and cameras allow observation and recording of lofting packed beds of spheres as the gas expansion wave reaches the upper surface of the bed.

Figure 1 (taken from Anilkumar et al (1993)) shows initial mobilisation of the bed, with fractures dividing the bed into slabs being the first visible feature after bed expansion. Tellingly, Anilkumar (1989, p.27) notes that “initial bed expansion occurs along horizontal fractures that ...partition the bed into slabs”. There is some variability of slab size, but typically each slab is ten to twenty particle diameters thick. The dynamics of the subsequent two-phase accelerating flow are complex, with particles falling from the bases of slabs and partitioning the fracture regions into bubbles, while particles at the tops of slabs are stable.

Slab thicknesses are observed to be approximately proportional to the square root of sphere diameter (Anilkumar, 1989), and this relationship is not hitherto

understood. They are also observed to be independent of the initial over-pressure, considering two pressures, 2 and 3.1 barg. Slabs are the first-observed features of bed fragmentation in all experiments, and they are central to any major heterogeneity that may be seen later in the flow sequence. The reason they occur is unknown, and has been speculated to perhaps be due to an instability in the high-density two-phase flows that subsequently develop (Anilkumar, 1989; Dartevell and Valentine, 2007). However, the fractures giving slabs are the very first observed change in the bead beds, suggesting the cause may lie in the interaction of the compressible gas flow with the stationary bead bed.

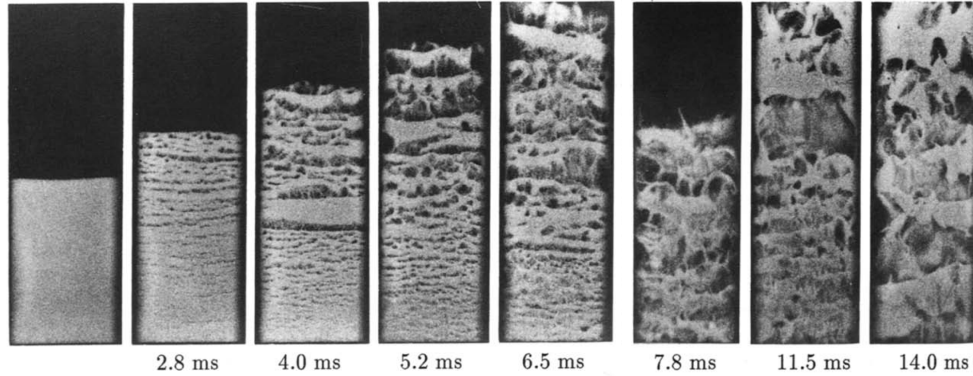


Fig. 1. Initiation of lofting of a bed of glass beads of depth 60cm, initially at rest on a solid base, from Anilkumar et al (1993, Fig. 2). Initial overpressure is 2.1 bar, and bead diameter is $125\mu\text{m}$. The time since arrival of the expansion wave at the bed surface is shown below each snapshot, which is a view of the bed from the side. The camera view is shifted upwards once, at a time between 6.5 and 7.8ms. We are grateful to Dr. Anilkumar for permission to reproduce this figure.

When smaller (38 and $95\mu\text{m}$ diameter) spheres are used together with smaller pressure changes (Cagnoli et al, 2002), slabs are still seen when pressure differences are small, but are not as ubiquitous as in the work of Anilkumar (1989). Only bubbles are observed at very small pressure differences; at larger values there is a bubbly region in the upper part of the sample, then a slab region between the bubbly region and the undisturbed base.

Anilkumar et al (1993) and Anilkumar (1989) also experiment with various arrangements of two or three layers of beads, either of the same size but different density, or of the same density but different sizes. Cracks starting near the top of the bed are still the first visible change upon depressurization, in all configurations, but whether the cracks survive longer term or not depends on the bed configuration, and in the stable configurations Anilkumar refers to repacking of

the layers that form initially, due to inertial or flow factors.

They find that if the lighter beads overly the heavier, the bed is unstable and slabs are ubiquitous and persistent in time, and the different layers separate first as primary slabs with larger void spaces between. The reverse bead arrangement with heavier ones on top leads initially to cracks forming, but then closing up so that eventually the entire bed lifts off as one plug, and remains very stable, with beads falling off from the bottom of the plug. If smaller beads overly larger beads, all of the same density, the bed is unstable and the layers of different sized beads separate from each other before themselves fragmenting into thinner slabs. An example of this from Anilkumar et al (1993) is reproduced in Fig. (2), and may be contrasted with the stable bead-size arrangement illustrated in Fig. (3) from the same paper. Well-mixed beds with three different bead sizes behave like a single-sized bead bed at the median bead size — slabs form and then separate.

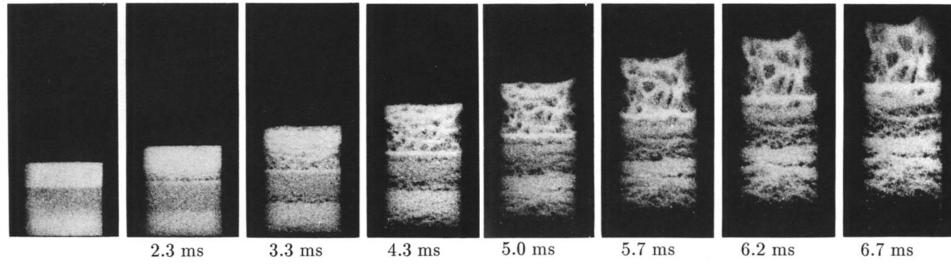


Fig. 2. Initiation of lofting of a bed of glass beads of depth 3.8cm, initially at rest on a porous mesh screen base, with high-pressure gas below, in and above the bed, from Anilkumar et al (1993, Fig. 4b). Initial overpressure is 2.1 bar, and beads are unstably layered with smallest diameter ($250\mu\text{m}$) in the upper one-third of the bed, middle diameter ($500\mu\text{m}$) in the centre one-third of the bed, and the largest diameter ($750\mu\text{m}$) in the lower one-third. The time since arrival of the expansion wave at the bed surface is shown below each snapshot. We are grateful to Dr. Anilkumar for permission to reproduce this figure.

Our aim in this paper is to explain the initial crack or slab formation in stationary beds of beads, seen in shock-tube experiments, and to explain the dependence of slab thickness on bead diameter. Subsequent flow development and repacking of certain configurations is beyond the scope of this paper.

3. Mathematical Model of Erupting Dusts

We consider the one-dimensional adiabatic upward compressible flow of gas through a deformable porous medium, the weakly cohesive stationary bed of beads. This leads to a nonlinear diffusion equation for gas pressure or density,

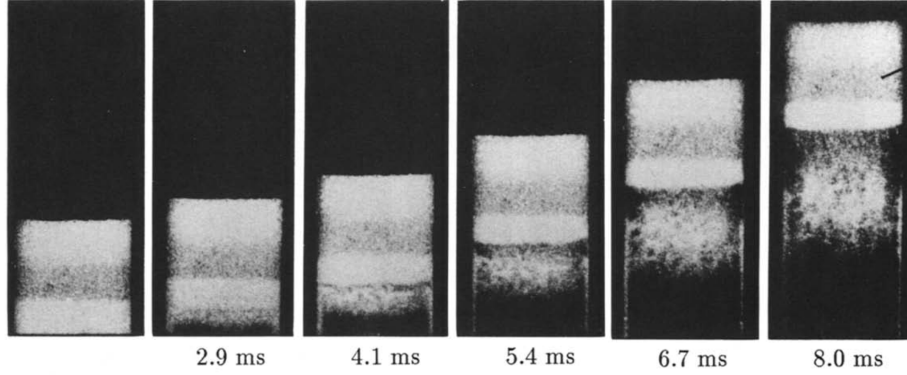


Fig. 3. Initiation of lofting of a bed of glass beads of depth 3.8cm, initially at rest on a porous mesh screen base with high-pressure gas below, in and above the bed, from Anilkumar et al (1993, Fig. 4a). Initial overpressure is 2.1 bar, and beads are stably layered with smallest diameter ($250\mu\text{m}$) in the lower one-third of the bed, middle diameter ($500\mu\text{m}$) in the centre one-third of the bed, and the largest diameter ($750\mu\text{m}$) in the upper one-third. The time since arrival of the expansion wave at the bed surface is shown below each snapshot. Layers that form initially upon bed expansion are not readily visible in these reproductions, and are reported to repack and disappear during upwards movement. We are grateful to Dr. Anilkumar for permission to reproduce this figure.

driven by a falling pressure at the upper surface of the bed, and a boundary value problem that determines the strain or stress in the weakly cohesive bead bed. We solve and find where the effective stress exceeds bed cohesion. The approach taken here is based on that used recently when modelling the fragmentation of competent rock samples when suddenly depressurized (Fowler et al., 2009; McGuinness et al., 2012), which in turn is based on seminal work by Biot (1956, 1962).

We make no attempt to model the flow of gas in the open chamber above the bead bed. We have experimental data showing that an exponential decay of pressure at the surface of the bead bed is a good approximation, so we use that as a boundary condition, and this allows us to focus here on the pressure evolution solely within the bed.

3.1. Dimensional Model Equations

Momentum conservation in the gas gives (Fowler et al., 2009)

$$\rho \phi v_t = -\phi p_z - A - D, \quad (1)$$

where z is the vertical coordinate (m) with origin at the base of the bed of beads, p is gas pressure, ρ is gas density, v is gas velocity, and v_t is gas acceleration. Typical values and ranges of values for material properties are listed in Table (1). The

porosity is $\phi(z, t)$, and for a packed bed of stationary spheres in contact with each other it has the initial value $\phi_0 \approx 0.4$, independent of sphere radius (Coelho et al, 1997). The term A accounts for an added mass effect, which corresponds physically to the concept that moving a solid sphere through gas requires displacing the gas backwards (Biot, 1956). It can be written

$$A = (1 - \phi)C_{VM}\rho(v_t - w_t), \quad (2)$$

where C_{VM} is an order one constant relating the added mass density to the porosity and gas density. A discussion of the use and value of C_{VM} in the case of dispersed flows may be found in Fowler et al. (2009). The exact value is not important in our development, as this term will be found to be negligible, later in this paper. w is the displacement of the solid beads, averaged over a representative elementary volume. The term D has dimensions of pressure gradient and accounts for the interfacial drag when gas moves past solid particles, and when Darcy's law for flow in a porous medium is extended to Forcheimer's or Ergun's equation Ergun (1952) to include turbulent flow effects, takes the form

$$D = \frac{\eta\phi^2}{k}(v - w_t) + \frac{\rho C_F \phi^3}{\sqrt{k}}(v - w_t)|v - w_t|, \quad (3)$$

where η is the dynamic viscosity of the gas (about $18 \times 10^{-6} \text{Pa.s}$), k is the permeability of the bed (about 10^{-10}m^2), and C_F is the dimensionless Ergun coefficient (about 0.5).

Momentum conservation for the solid beads gives

$$\rho_s(1 - \phi)w_{tt} = (1 - \phi)\sigma_z + A + D - \rho_s(1 - \phi)g - F, \quad (4)$$

where F accounts for friction at the walls of the container, and is taken to be initially of the form appropriate for static friction,

$$F = \frac{\mu_f w}{C_c D_p}, \quad (5)$$

with μ_f an effective shear modulus for the bed, and C_c the length of the perimeter of the container cross-section. We set the effective shear modulus to the same value as the elastic modulus E , acting over a distance of one bead diameter, taking the walls to be in stick mode initially, before slip occurs. We have assumed the initial value of displacement w is zero. There is no dependence on normal force in this formulation, since the normal force only provides a criterion for the transition

to sliding friction (which does depend on normal force), not for the value of static (non-slip) frictional force exerted by the walls on the bed.

The second-last term on the right-hand side of eqn. (4) is called the overburden, and is negligible in Fowler et al. (2009) but is expected to play a central role at the lower over-pressures considered here for erupting dust experiments.

The term σ is the vertical component of solid stress in the beads averaged over the cross-section, as detailed in Fowler et al. (2009), so that the stress-strain relationship is

$$(1 - \phi)\sigma = Ew_z - \alpha p , \quad (6)$$

where E is an elastic constant, and α is an order one elastic constant (Fowler et al., 2009).

The permeability of a bed of packed uniform spheres of diameter D_p is the subject of the Karman-Cozeny relationship,

$$k = \frac{D_p^2 \phi^3}{72\tau(1 - \phi)^2} , \quad (7)$$

where τ is tortuosity. Coelho et al (1997) note that in a survey of a number of different experiments on packed beds, k is observed to be in the range $(2-3) \times 10^{-3} D_p^2 / 4 \text{ m}^2$ before bed expansion or fluidisation occurs. We here use

$$k = 0.625 \times 10^{-3} D_p^2 \quad (8)$$

for the permeability of the packed bed before any movement of beads occurs.

Conservation of gas mass gives

$$(\rho \phi)_t + (\rho \phi v)_z = 0 , \quad (9)$$

and assuming adiabatic expansion of the gas, we can relate gas pressure $p(z, t)$ and density as

$$\rho = \rho_0 \left(\frac{p}{p_0} \right)^{\frac{1}{\gamma}} , \quad (10)$$

where γ is the adiabatic index, with value 1.4 for nitrogen, and ρ_0 and p_0 are the initial values of gas density and pressure, before the diaphragm is ruptured in the shock tube.

The simplifying assumption of adiabatic gas expansion is based on the relatively long timescale for conductive heat transport into a glass bead. This timescale ranges from 5–125 milliseconds for beads of diameter ranging from 100–500 μm .

While the shock-tube experiments operate on a time scale of milliseconds, bed rupture will be seen in our model to occur much faster, on a timescale of microseconds. Hence the timescales we are interested in are much shorter than the time scales for thermal transport between gas and beads.

Mass conservation for the beads can be expressed in the form

$$(\rho_s(1 - \phi))_t + (\rho_s(1 - \phi)w_t)_z = 0 , \quad (11)$$

but as in Fowler et al. (2009) this is considered to be satisfied in the following, by requiring constant $\phi = \phi_0$ and small displacements w , so is ignored in the remainder of this paper.

The initial conditions are $v = 0$, $-\sigma = p = p_0$, $w = w_t = 0$, $\phi = 0.4$ at $t = 0$. The boundary conditions are $v = w = 0$ at the lower end of the bed $z = 0$; and at the upper surface $z = l$ of the bed, pressure reduces with time as the expansion wave hits, modelled as

$$-\sigma = p = p_c(t) = (p_0 - p_a) \exp(-t/t_c) + p_a , \quad (12)$$

where t_c is the timescale for pressure decay from the initial value p_0 to atmospheric pressure p_a at the bed surface, about 1 ms for the shock tube used by Anilkumar et al (1993).

3.2. Rupture

The gas pressure will drop at the surface of the bed from time zero when the expansion wave arrives there, and this pressure drop will penetrate the bed, so that for a time an increasing gas pressure difference will develop, between gas pressure in the bed and gas pressure at the surface. This pressure difference drives a change in stress in the solid, which increases until rupture of the bed occurs.

The bed is assumed to be held in place by

1. gravity (the overburden, or weight of the solid beads),
2. an intrinsic cohesion S_0 , and
3. friction at the walls of the bed container.

Gravity and friction are already allowed for in the solid momentum conservation equation. Then, as in Fowler et al. (2009), the bed is taken to rupture when the effective stress $(1 - \phi)(\sigma + p)$ exceeds the intrinsic cohesion S_{0c} .

3.3. Cohesion

Granular materials have an intrinsic cohesion or tensile strength due to Lifschitz-van der Waals forces, that varies with bead diameter (e.g., Xu & Zhu (2006); Weir (1999); Jaraiz et al (1992); Tanneur et al (2008)). Glass beads in the size range we are considering are classified as Geldart Group A and B powders (Geldart, 1973; Jaraiz et al, 1992), which are readily fluidised, and where gravity effects are larger than Lifschitz-van der Waals interparticle forces, although for Group A powders these interparticle forces still play a part. The transition to Group B powders with larger beads, where interparticle forces are much smaller than gravity, occurs at about $100\mu\text{m}$ diameter for glass beads in the absence of factors like moisture altering cohesion.

There remain discrepancies between theoretical and measured values of cohesion for Group A and B powders. We present in the Appendix a discussion focussed on finding a reasonable range of possible values for the cohesion of the glass beads under consideration, with diameters of 125, 500 and $750\mu\text{m}$. The results of this discussion are briefly presented here.

The criterion for bed rupture is given in terms of the effective cohesion S_{0c} of a possibly consolidated bed as

$$(1 - \phi)(\sigma + p) > S_{0c} \quad (13)$$

where

$$S_{0c} = \sigma_{0c} + \sigma^0 = \sigma_0 + \kappa\sigma_{N0} + \sigma^0 \quad (14)$$

where the consolidated cohesion due to non-geometric effects is

$$\sigma_{0c} = \frac{(1 - \phi)N_k(\phi)}{\pi D_p^2} H = \sigma_0 + \kappa\sigma_{N0} \text{ Pa} . \quad (15)$$

where compression gives rise to the term

$$\kappa\sigma_{N0} = \kappa\sigma_{NC0} + \kappa(1 - \phi)\rho_s g l(1 - z) \approx (9 - 600) + 670(1 - z) \text{ Pa} . \quad (16)$$

where σ_{NC0} is due to any prior compression the bed has experienced, the second term on the right-hand side is compression due to overburden, and where the effective geometric cohesion is given by $\sigma^0 = (1 - \phi)\rho_s g D_p/2$.

3.4. Nondimensional Model Equations

The dimensional model equations are rescaled and nondimensionalized to variables with a tilde on top, by the transformations

$$\begin{aligned}
\rho &= \rho_0(1 - \lambda\tilde{\rho}) , & p_c &= p_0(1 - \gamma\lambda\tilde{p}_c) \\
p &= p_0(1 - \gamma\lambda\tilde{p}) , & p_a &= p_0(1 - \gamma\lambda\tilde{p}_a) \\
z &= l\tilde{z} , & \sigma &= p_0(1 - \gamma\lambda\tilde{\sigma}) \\
t &= t_0\tilde{t} , & t_0 &= \frac{\lambda l}{v_0} \\
v &= v_0\tilde{v} , & v_0 &= \frac{k_0\rho_s(1-\phi_0)g}{\eta\phi_0} \\
k &= k_0\tilde{k} , & k_0 &\approx 1.6 \times 10^{-10} \text{m}^2 \\
w &= w_0\tilde{w} , & w_0 &= \frac{p_0\gamma\lambda l}{E} \\
A &= A_0\tilde{A} , & A_0 &= \frac{\rho_0 v_0^2}{\lambda l} \\
D &= D_0\tilde{D} , & D_0 &= \frac{p_0\gamma\lambda}{l} \\
\lambda &= \frac{(1-\phi_0)\rho_s g l}{\gamma p_0}
\end{aligned} \tag{17}$$

Pressure changes have been scaled on overburden pressure relative to the initial gas pressure, through the parameter λ , and velocity scale is chosen to simplify the drag term that dominates the interaction between gas and solid phases.

The resulting dimensionless equations are

$$\nu_1\phi(1 - \lambda\tilde{\rho})\tilde{v}_{\tilde{t}} = \phi\tilde{p}_{\tilde{z}} - \nu_1\tilde{A} - \tilde{D} \tag{18}$$

$$[(1 - \lambda\tilde{\rho})\phi]_{\tilde{t}} = -\frac{\partial}{\partial\tilde{z}} [\lambda(1 - \lambda\tilde{\rho})\phi\tilde{v}] \tag{19}$$

$$\varepsilon(1 - \phi)\tilde{w}_{\tilde{t}} = -(1 - \phi)\tilde{\sigma}_{\tilde{z}} + \nu_1\tilde{A} + \tilde{D} - G - \lambda_f\tilde{w} \tag{20}$$

$$(1 - \phi)(1 - \gamma\lambda\tilde{\sigma}) = \gamma\lambda\tilde{w}_{\tilde{z}} - \alpha(1 - \gamma\lambda\tilde{p}) , \tag{21}$$

$$\tilde{A} = (1 - \phi)C_{VM}(1 - \lambda\tilde{\rho})(\tilde{v}_{\tilde{t}} - \delta\tilde{w}_{\tilde{t}}) \tag{22}$$

$$\begin{aligned}
\tilde{D} &= \frac{\phi^2}{\phi_0} \left(\frac{\tilde{v} - \delta\tilde{w}_{\tilde{t}}}{\tilde{k}} \right) \\
&\quad + \text{Re}_{pCF} \frac{\phi^3}{\phi_0} (1 - \lambda\tilde{\rho}) \left(\frac{(\tilde{v} - \delta\tilde{w}_{\tilde{t}})|\tilde{v} - \delta\tilde{w}_{\tilde{t}}|}{\sqrt{\tilde{k}}} \right)
\end{aligned} \tag{23}$$

$$G = \frac{1 - \phi}{1 - \phi_0} \tag{24}$$

with the first three equations representing conservation of gas momentum, gas mass, and solid momentum respectively. Dimensionless pressure at the surface of the bed satisfies

$$\tilde{p}_c = \tilde{p}_a(1 - \exp(-a\tilde{r})) ,$$

and parameters and their typical values are listed in Table (2).

Symbol	Meaning	range	Typical value
C_c	perimeter of container		0.15m
c_F	Ergun coefficient		0.5
C_{VM}	added mass const		1
D_p	bead diameter	30–1000 μ m	500 μ m
E	elastic constant		10 ¹¹ Pa
k_0	permeability scale	4–40 $\times 10^{-11}$ m ²	1.6 $\times 10^{-10}$ m ²
l	bed depth	0.15–0.64 m	0.15 m
p_0	initial gas pressure	2–3 bara	3 bara
t_c	chamber relaxation time		1 ms
η	gas viscosity		1.8 $\times 10^{-5}$ Pa s
γ	specific heat ratio		1.4
ρ_0	initial gas density	1–2.3 kg.m ⁻³	2.3 kg.m ⁻³
ρ_s	solid density (glass)		2.5 $\times 10^3$ kg m ⁻³
μ_f	friction shear modulus		10 ¹¹ Pa
ϕ_0	initial porosity		0.4

Table 1. Typical values of the physical constants of the model. The gas properties are those of nitrogen at room temperature.

The adiabatic law becomes

$$1 - \lambda\tilde{p} = (1 - \lambda\gamma\tilde{p})^{1/\gamma} . \quad (25)$$

The bed rupture condition (13) becomes

$$(1 - \phi) [p_0(1 - \gamma\lambda\tilde{\sigma}) + p_0(1 - \gamma\lambda\tilde{p})] > S_{0c} , \quad (26)$$

and using eqn (21) this becomes

$$p_0\gamma\lambda\tilde{w}_z + (1 - \beta)p_0(1 - \gamma\lambda\tilde{p}) > S_{0c} , \quad (27)$$

Parameter	Formula	Typical value
a	$\frac{t_0}{t_c}$	2.5
Re_p	$\frac{\rho_0 v_0 \sqrt{k_0}}{\eta}$	0.5
t_0	$\frac{\lambda l}{v_0}$	2.5 ms
v_0	$\frac{k_0 p_0 \gamma \lambda}{\eta \phi_0 l}$	0.3 m/s
β	$\alpha + \phi_0$	1
δ	$\frac{p_0 \gamma}{E}$	4×10^{-6}
ϵ	$\frac{\rho_s v_0^2}{E \lambda^2}$	9×10^{-5}
λ	$\frac{(1-\phi_0) \rho_s g l}{\gamma p_0}$	0.005
λ_f	$\frac{\mu_f l^2}{C_c D_p E}$	308
ν_1	$\frac{\rho_0 v_0^2}{p_0 \gamma \lambda^2}$	0.02

Table 2. Definitions and typical values of the parameters of the model.

where $\beta \equiv \phi + \alpha = O(1)$ so that approximately, rupture occurs when

$$\tilde{w}_{\tilde{z}} > \tilde{S}_{0c} \equiv \frac{S_{0c}}{p_0 \gamma \lambda} . \quad (28)$$

We now drop the tilde notation, so that unless otherwise stated, variables are dimensionless from now on.

3.5. Reduced Equations for Rupture

Since λ is small, the adiabatic law (25) may be approximated as

$$p = \rho .$$

Considering the initiation of movement of beads, we set $\phi = \phi_0$ constant everywhere. Then neglecting terms containing the small parameters ν_1 , δ , and ϵ , we obtain the reduced set of dimensionless equations

$$\phi_0 p_z = D \quad (29)$$

$$p_t = v_z \quad (30)$$

$$(1 - \phi_0)\sigma_z = D - 1 - \lambda_f w \quad (31)$$

$$(1 - \phi_0)(1 - \gamma\lambda\sigma) = \gamma\lambda w_z - \alpha(1 - \gamma\lambda p), \quad (32)$$

$$D = \phi_0 \frac{v}{k} + \text{Re}_p c_F \phi_0^2 \frac{v^2}{\sqrt{k}}. \quad (33)$$

The last equation may be further simplified by noting that $\text{Re}_p c_F \phi_0 \approx 0.1$ is relatively small, so that $D \approx \phi_0 v/k$. This in combination with eqns (29) and (30) gives the linear diffusion equation for nondimensional gas flow,

$$p_t = (kp_z)_z, \quad (34)$$

with boundary conditions $p_z = 0$ at $z = 0$, and $p = p_c(t) = p_a(1 - \exp(-at))$ at $z = 1$, and initial condition $p = 0$. A typical nondimensional value for p_a is 90.

The steady-state solid momentum equation (31) combined with a differentiated stress-strain equation (32) gives the following nondimensional boundary-value problem for solid displacement w ,

$$w_{zz} - \lambda_f w = -\beta p_z + 1, \quad (35)$$

with boundary conditions $w = 0$ at $z = 0$, and $w_z = 0$ at $z = 1$. We will use $\beta = 1$. Strain in the solid is driven by gas pressure changes through the term p_z , and by overburden through the term 1.

The reduced problem has separated into two problems, the first being a soluble linear pressure diffusion equation. The second, boundary-value problem, may be solved to find w once pressure is known from the solution to the diffusion problem. Then the rupture condition (28) can be checked at each value of time, to find out when and where the first bed rupture occurs.

4. Solutions

We now consider analytic and numerical solutions, firstly to the gas diffusion problem in equation (34), and secondly to the boundary-value problem (35).

4.1. Diffusion Equation Solutions

We solve the linear diffusion problem (34) with a constant scaled permeability $k = 1$, corresponding to a bed of beads of uniform diameter. Taking a Laplace transform in time gives

$$P(z, s) = \int_0^\infty p(z, t) e^{-st} ds$$

reduces the problem to the ordinary differential equation

$$P_{zz} = sP$$

with boundary conditions $P_z = 0$ at $z = 0$, $P = \frac{ap_a}{s(s+a)}$ at $z = 1$. The solution in transform space is

$$P = \frac{ap_a}{s(s+a)} \frac{\cosh(\sqrt{s}z)}{\cosh(\sqrt{s})}. \quad (36)$$

Inverting this is possible by an extension of work presented in Crank (1975, eqn 2.53), and gives an infinite sum of erfc functions, which converges rapidly for all except large values of t . A small-time expansion follows from a consideration of the large- s expansion of P , as

$$P \sim ap_a \left(\frac{\exp(-\sqrt{s}(1-z))}{s^2} \right), \quad s \rightarrow \infty \quad (37)$$

with inverse transform (Abramowitz & Stegun, 1972, 29.3.86)

$$p = 4ap_a t \, i^2 \operatorname{erfc} \left(\frac{1-z}{2\sqrt{t}} \right), \quad (38)$$

where $i^2 \operatorname{erfc}$ is an integrated error function:

$$i^2 \operatorname{erfc}(x) = \frac{1}{\sqrt{\pi}} \int_x^\infty (t-x)^2 e^{-t^2} dt.$$

This approximation to the solution, expected to be valid for early to moderate times, can also be written in the form

$$p = ap_a \left[\left(t + \frac{(1-z)^2}{2} \right) \operatorname{erfc} \left(\frac{1-z}{2\sqrt{t}} \right) - (1-z) \sqrt{\frac{t}{\pi}} e^{-\frac{(1-z)^2}{4t}} \right], \quad (39)$$

where

$$\operatorname{erfc}(x) \equiv \frac{2}{\sqrt{\pi}} \int_x^\infty e^{-t^2} dt.$$

Numerical solutions, comparing the above asymptotic approximation with full numerical solutions of the linear diffusion equation, confirm that this is an excellent approximation for early times, as illustrated in Fig. (4), where the pressure difference $\Delta p = p_c - p$ is plotted against z , for five dimensionless times stepping evenly from zero to 2×10^{-6} and a bead diameter of $500 \mu\text{m}$.

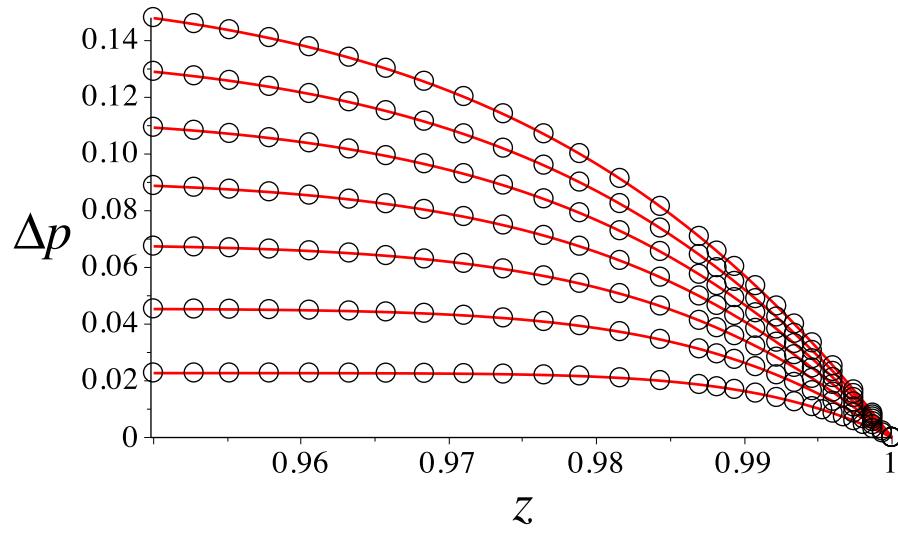


Fig. 4. Numerical solutions p to the gas diffusion equation (34) with $k = 1$, obtained using the `pdsolve` command in Maple, and converted to the form $\Delta p = p_c - p$, plotted against nondimensional bed height z , for nondimensional times evenly spaced from zero to 7×10^{-4} . Since $t_0 = 0.0025$ s, the dimensional time is up to 1.8×10^{-6} s. The plot shows the excellent match between numerical solutions (solid line) and the analytical early-time approximation given by equation (38) (circles).

4.2. Boundary-Value Solutions

Following McGuinness et al. (2012), we solve the boundary-value problem (35) for solid strain w_z with $\beta = 1$, given the early-time pressure solution (38).

The Green's function $G(z, z_0)$ for solving

$$w_{zz} - \lambda_f w = 1 - p_z$$

with p_z prescribed as a function of z at a given time, and boundary conditions $w(0) = 0$, $w_z(1) = 0$, satisfies

$$G_{zz} - \lambda_f G = \delta_D(z - z_0)$$

where δ_D is the Dirac delta function, with the usual continuity conditions across the jump at $z = z_0$. G is given by the formula

$$G(z, z_0) = -\frac{1}{\nu D} \begin{cases} \sinh(\nu z) \cosh(\nu(1 - z_0)), & z \leq z_0 \\ \sinh(\nu z_0) \cosh(\nu(1 - z)), & z > z_0 \end{cases}, \quad (40)$$

where $D = \cosh \nu$ and $\nu = \sqrt{\lambda_f}$.

Then w_z is obtained by the quadrature

$$w_z(z) = \int_0^1 G_z(z, z_0) [1 - p_z(z_0)] dz_0, \quad (41)$$

where the derivative of the Green's function is

$$G_z(z, z_0) = -\frac{1}{D} \begin{cases} \cosh(\nu z) \cosh(\nu(1 - z_0)), & z \leq z_0 \\ -\sinh(\nu z_0) \sinh(\nu(1 - z)), & z > z_0 \end{cases} \quad (42)$$

This formula has been tested in Matlab by comparing with a direct numerical solution to (35) using the routine `bvp4c`.

Numerical solutions for w_z computed using the quadrature (41) and the pressure solution (37) with typical parameter values, are plotted in Fig. (5). The value $\lambda_f = 308$ is large enough that the outer solution $w \sim -(1 - p_z)/\lambda_f \ll 1$ obtained by dividing through by λ_f and neglecting w_{zz} is the solution over much of the z range, giving a small positive value for w_z .

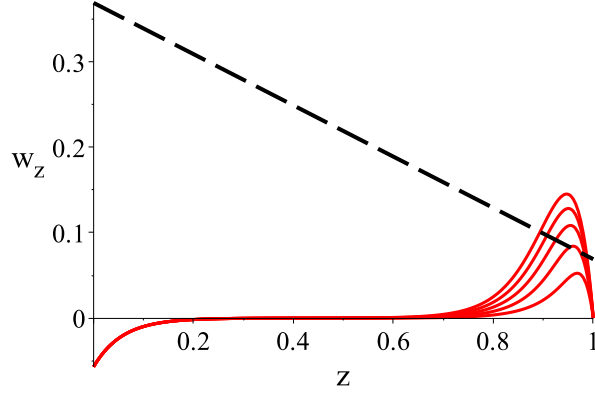


Fig. 5. Strain w_z versus z (solid lines), at evenly spaced dimensionless times from zero to $t = 25 \times 10^{-4}$, compared with the rescaled tensile strength (dashed line). Parameter values are as listed in Tables (1) and (2). Strain increases with time. Bed rupture is observed at about $t = 10 \times 10^{-4}$, when w_z first exceeds the cohesion. This corresponds to a dimensional time of about $2.5\mu\text{s}$

4.3. The Shape of Strain Solutions

To allow the model to be applied to a range of situations, with varying bed permeability and/or bead density, the shape of solutions w_z will be explored using singular perturbation theory. The large size of λ_f will be leveraged; small values are perturbations of the zero friction case discussed in the next subsection.

The boundary-value problem is considered in the form

$$\epsilon^2 w_{zz} - w = \epsilon^2(1 - p_z)$$

where $\epsilon^2 = 1/\lambda_f \ll 1$ is small.

The outer solution is a good approximation to w whenever the second derivative term can be ignored, and is small:

$$w^{\text{outer}} = \epsilon^2(p_z - 1) \approx 0,$$

giving the positive but small outer solution for strain

$$w_z^{\text{outer}} = \epsilon^2 p_{zz} \approx 0.$$

Inner solutions occur near $z = 0$ and near $z = 1$. Near $z = 0$, we rescale $z = \epsilon z^*$ so that z is close to zero and p_z is approximated by $p_z(0)$ which is zero,

$$w_{z^* z^*}^{\text{inner1}} - w^{\text{inner1}} \approx \epsilon^2(1 - p_z(0)) = \epsilon^2.$$

Solving this with $w(0) = 0$ and requiring it to match the outer solution gives

$$w^{\text{inner1}} = \epsilon^2(e^{-z/\epsilon} - 1) ,$$

giving the strain near $z = 0$ as

$$w_z^{\text{inner1}} = -\epsilon e^{-z/\epsilon} ,$$

which explains the small uptick seen in w_z near origin in Fig (5).

Near $z = 1$, we rescale $\epsilon z^* = 1 - z$, and we acknowledge the importance of the p_z term by taking it to be large, as $p_z = \frac{\tilde{p}_z}{\epsilon^2}$, giving

$$w_{z^*z^*}^{\text{inner2}} - w^{\text{inner2}} \approx \epsilon^2 - \tilde{p}_z(z) \approx -\tilde{p}_z(z) .$$

This is the same as the boundary value problem that arises in Fowler et al. (2009) when rupturing competent rock (noting that there is a sign difference between the scaled pressures used). There a powerful iterative general argument is given for the shape of w_z^{inner2} having a unique maximum, as seen near $z = 1$ in Fig (5).

These arguments that w_z has the general shape seen in Fig (5) apply for general shapes of $p(z)$ that are monotonic increasing, so that the unique local maximum in w_z that rises to meet a threshold cohesion is common to a range of modelling situations, in particular if permeability k is allowed to vary with depth, since the shape of $p(z)$ would be similar.

4.4. No Wall Friction

Solutions to the boundary-value problem (35) are particularly straightforward if wall friction is ignored, that is, $\lambda_f = 0$. Then

$$w_{zz} = 1 - p_z$$

which can be integrated from z to 1, to get

$$w_z = p_c - p + z - 1 , \tag{43}$$

with rupture condition

$$w_z > S_{0c} , \tag{44}$$

so that rupture occurs when

$$p_c - p > 1 - z + S_{0c} .$$

That is, in the absence of wall friction, there is a nice physical interpretation of the rupture condition, that bed rupture is predicted to occur when the difference between the gas pressure at depth z and the gas pressure p_c at the surface of the bed matches the overburden $1 - z$ (in nondimensional form) at that depth, plus the effective cohesion, S_{0c} .

This rupture is illustrated for the choice $\sigma_{NC0} = 500$ in Fig. (6), where it can be seen that w_z has a unique local maximum due to the combination of a monotonically decreasing $p_c - p$, and a monotonically increasing $z - 1$, as z increases.

This behaviour for strain differs from that for the rupture of competent rocks found in Fowler et al. (2009) and McGuinness et al. (2012), where the effect of glue or a tight fit at the walls of the shock tube was crucial to obtaining a local maximum in w_z , and hence obtaining fragmentation at some finite depth rather than at the bottom of the sample. In contrast, w_z has a local maximum now with zero wall friction. The difference here is that gravity or overburden is important, giving the crucial $z - 1$ term, whereas gravity was correctly neglected in Fowler et al. (2009) due to the relatively larger over pressures required to overcome the tensile strength of competent rock.

In regions away from $z = 1$, where the pressure has not had time to change yet, $w_z \approx z - 1 + p_c$ in this zero wall friction case, straight lines of slope one, moving upwards as p_c increases with time, as illustrated in Fig. (7) by the bottom-most line, and as suggested by the smaller z values in Fig. (6).

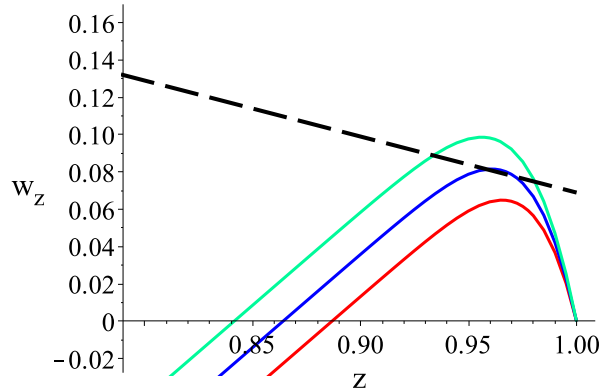


Fig. 6. Strain w_z versus z (solid lines), at dimensionless times $t = 3, 4, 5 \times 10^{-4}$, compared with the tensile strength (dashed line). Wall friction is set to zero, and other parameter values are as listed in the tables. Strain increases with time. Bed rupture is observed at dimensionless values $t \approx 4 \times 10^{-4}$, and $z \approx 0.974$.

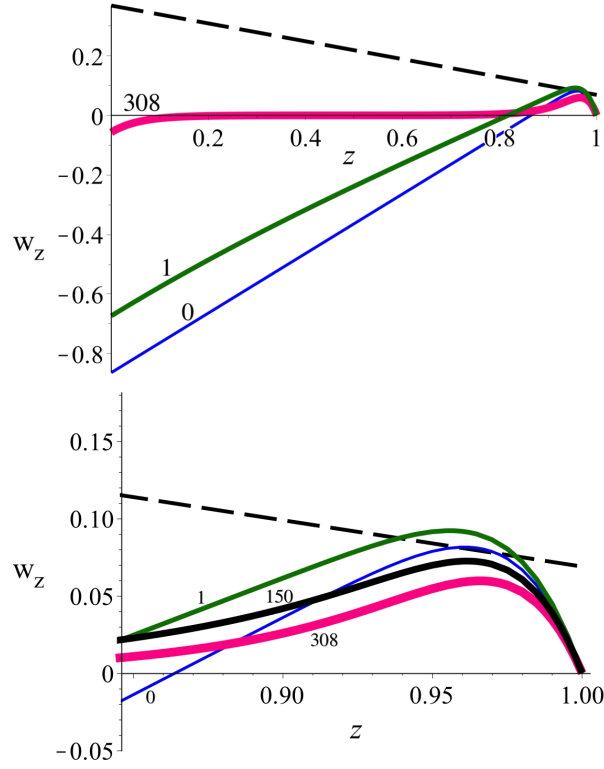


Fig. 7. Strain w_z versus z , at dimensionless time $t = 6 \times 10^{-4}$, compared with the tensile strength (dashed line). Wall friction is set to $\lambda_f = 0, 1, 308$ (solid lines) in the first plot, with thicker lines for higher friction values. Other values are as listed in the tables. Strain increases with wall friction, away from $z = 1$. The second plot shows a close-up of z near one, with an extra $\lambda_f = 150$ value included — this value was not different enough to $\lambda_f = 308$ to show in the first plot. λ_f values are indicated near the associated curves.

The effect of varying the friction term between zero and 308 is explored in Fig. (7), where w_z is graphed versus z , for one value of time and several values of λ_f . It can be seen that while the effect of varying friction is noticeable away from $z = 1$, it is relatively small near $z = 1$. There is a delay in rupture times as λ_f increases, but the location of the rupture is not very sensitive to λ_f . This is emphasised in Fig. (8), where the time of rupture is a little later with wall friction, but the location of rupture is almost indistinguishable from the zero wall friction case.

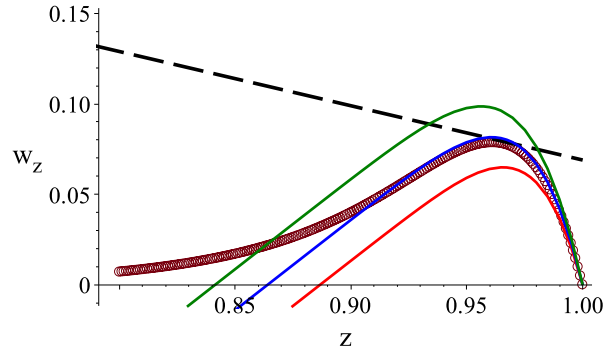


Fig. 8. A comparison of the dimensionless strain w_z computed for wall friction $\lambda_f = 308$ (circles) at dimensionless time $t = 9 \times 10^{-4}$, with a wall friction set to zero (solid lines) at times $t = 5, 6, 7 \times 10^{-4}$. The threshold for rupture is the dashed line. Rupture occurs at $t = 6 \times 10^{-4}$ for zero wall friction, at almost the same location as it occurs for nonzero wall friction but at a different time.

5. Varying Bead Size

The effect of varying bead size on the size of the layers formed is explored here, using the zero wall friction case, since it is simpler and the depth of rupture appears to be almost the same as for nonzero wall friction. The main effect of changing bead size in our modelling, is to change the permeability of the bed — porosity is unaffected. There is also an effect on the elevation of the eruption threshold due to increased effective tensile strength with reduced bead size, which will become more significant for bead sizes less than 100 microns as van der Waals' forces become significant.

A formula approximating the dependence of layer size on bead size and overpressure can be obtained by considering an even simpler asymptotic expansion of

the early time solution obtained by Laplace transforms in the previous section, by assuming $1 - z$ is small.

If the approximate transform (37) is further expanded for small $1 - z$, it becomes

$$P \sim ap_a \left(\frac{1 - \sqrt{s}(1 - z) + s(1 - z)^2/2}{s^2} \right), \quad z \rightarrow 1,$$

which inverts to give

$$p \sim ap_a \left(t - 2(1 - z) \sqrt{\frac{t}{\pi}} + \frac{(1 - z)^2}{2} \right), \quad z \rightarrow 1, t \rightarrow 0, 1 - z \ll \sqrt{t}.$$

Although this is a poor approximation for large $1 - z$, and it tends to under-predict layer sizes, it provides a good estimate of overall trends in layer size, as will be seen in what follows.

Rupture of the bead bed occurs (ignoring wall friction) when

$$p_c - p = 1 - z + S_{0c},$$

and when the slope of the pressure solution matches the slope of the overburden plus cohesion on the right-hand side of this equation, that is, there is just one root for the solution $1 - z$. These considerations, using the early time simplification $p_c \sim ap_a t$, lead to the following two simultaneous equations for time of rupture t_r and layer size $y = 1 - z$:

$$ap_a \left(2y \sqrt{\frac{t_r}{\pi}} - \frac{y^2}{2} \right) = S_{0c} + y, \quad (45)$$

$$ap_a \left(2 \sqrt{\frac{t_r}{\pi}} - y \right) = \frac{dS_{0c}}{dy} + 1. \quad (46)$$

Noting that

$$S_{0c} = \left(\frac{1}{p_0 \gamma \lambda} \right) \left(\frac{10^{-7}}{D_p^2} + \beta_4 D_p + \kappa \sigma_{NC0} + \beta_5 y \right),$$

where $\beta_4 = (1 - \phi_0) \rho_s g / 2 \approx 7350$, and $\beta_5 = \kappa l \beta_4 \approx 670$, the solution to these two equations is

$$y = \sqrt{\frac{2}{ap_a p_0 \gamma \lambda} \left(\frac{10^{-7}}{D_p^2} + \beta_4 D_p + \kappa \sigma_{NC0} \right)}.$$

p_a is nondimensional, so using

$$a\tilde{p}_a = \frac{\lambda l \tilde{p}_a}{v_0 t_c} = \frac{l}{v_0 t_c \gamma} \left(\frac{p_0 - p_a}{p_0} \right) .$$

and

$$v_0 = \frac{k_0(1 - \phi_0)\rho_s g}{\eta \phi_0} ,$$

and noting that $k_0 = 0.625 \times 10^{-3} D_p^2$, we see that, in terms of purely dimensional variables, slab thickness $Y = ly$ (m) is given by

$$Y^2 = \beta_6 \left(\frac{p_0}{p_0 - p_a} \right) \left(10^{-7} + \beta_4 D_p^3 + \kappa \sigma_{NC0} D_p^2 \right) , \quad (47)$$

where

$$\beta_6 = \frac{1.25 \times 10^{-3} t_c \gamma}{\phi_0 \eta}$$

contains parameters independent of initial pressure and bead diameter.

Note that the layer size referred to here is the initial thickness of layers when cracks first form in the stationary bead bed, before they begin to move upwards and increase in size.

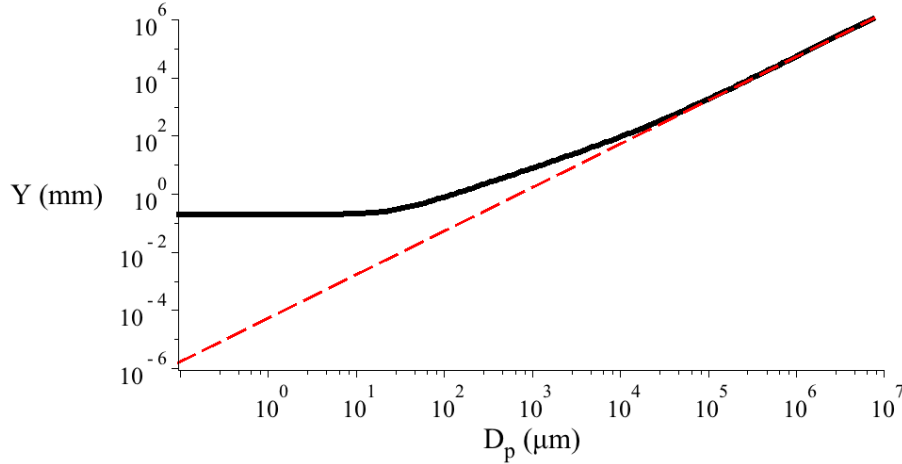


Fig. 9. Layer size (mm) versus bead diameter (μm) (solid line), according to the theoretical formula equation (47) with the choice $\sigma_{NC0} = 500$. Also shown in this plot (dashed line) is the large diameter approximation that layer size depends on diameter to the power 1.5.

The resulting theoretical dependence of slab size on bead diameter is graphed as a log-log plot in Fig. (9), and can be seen to have three different regions, with constant slab size at very small diameters, a slope of one indicating a linear relationship between layer size and diameter at moderate diameters including those considered here, and a slope of 1.5 for large diameters indicating a power law of 1.5. The reasons for the shape of this plot are explored in more detail in the next paragraph.

There are three terms in the formula for the dependence of Y^2 on bead diameter. Which one is dominant, varies depending on the value of bead diameter. For diameters less than about 30μ , the first term (due to σ_0 , unconsolidated Lifschitz-van der Waals forces) is dominant, and slab thickness is predicted to be constant, independent of bead diameter.

For diameters between 30μ and 1cm, the last (quadratic) term is dominant, and slab thickness is predicted to be linear in bead diameter, as observed in Fig. (10). This term is due to any prior consolidation that might have taken place in charging the shock tube to initial pressure p_0 . This has come about through the dependence of velocity on permeability which varies as the square of diameter. A simple explanation is that the similarity variable y^2/t reaches a critical value s_c at rupture, so that $y^2 \propto s_c t$, and time scales as $1/v \propto k \propto D_p^2$, giving $y \propto D_p$.

For diameters greater than 1cm, slab thickness is predicted to vary as diameter to the power 1.5, due to the middle (cubic) term in eqn 47. It arises from the term σ^0 , the geometric cohesion term.

The pressure normalization in this result (47) predicts that Y is not very sensitive to overpressure. For example, if the shock tube is 3 bars over atmospheric, $\Delta p = (4 - 1)/4 = 3/4$, while if the shock tube is 1 bar over atmospheric, $\Delta p = (2 - 1)/2 = 1/2$. Taking square roots gives a relative change of layer thickness Y from 3 bars to 1 bar as about 9%. This insensitivity is arguably consistent with the observations of Anilkumar (1989, Table 3.4), where no dependence of layer size on initial over-pressure was observed over this range of over-pressures.

The dependence of Y on bead diameter, according to this early-time, small $1-z$ approximate solution, is graphed in Fig. (10). As indicated by the approximate theoretical layer size (47), Y increases monotonically with bead diameter, despite the increased cohesion at small diameters. This increase is exactly offset by the decrease in permeability as diameter decreases. This behaviour is in very good agreement with experimental results, and provides validation of the modelling assumptions made in this paper.

Fig. (10) indicates that provided cohesion is taken to be large enough, a good agreement is obtained between experimental values of layer size, and layer sizes

predicted by our model. There is also good agreement between experimental values of layer size variations with bead size, and the layer size variations predicted by our model.

Note that for bead sizes between $30\mu\text{m}$ and 1cm , the model results predict that slab size varies linearly with bead diameter, and this is consistent with the data of Anilkumar. In his original work, it was speculated that layer size depends of the square root of bead diameter, which is also consistent with the data over the range of bead sizes considered. It would be useful to see further experimental data for smaller bead sizes, to more clearly distinguish between our model predictions and the posited square root behaviour, and to test the model prediction that slab size becomes constant for beads less than $30\mu\text{m}$.

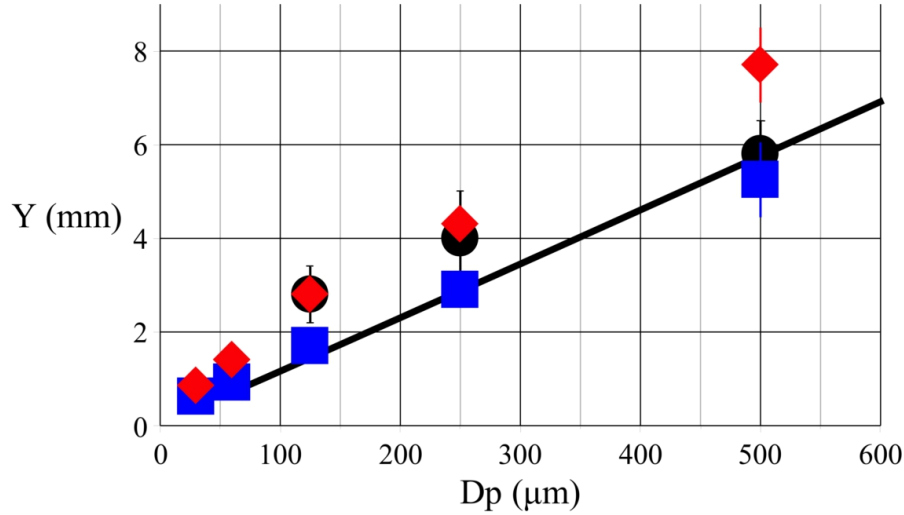


Fig. 10. Layer sizes at rupture versus bead diameter, showing the formula in the theoretical model equation (47) with the choice $\sigma_{NC0} = 1200$ (solid line), compared with Anilkumar's three experimental results (black disks, with error bars on them to indicate the measurement uncertainty of about $\pm 0.5\text{mm}$), and more accurate numerical values obtained by using equations (43) and (44), using $\sigma_{NC0} = 1000$ (red diamonds) and $\sigma_{NC0} = 500$ (blue solid squares).

6. Multiple Layers of Beads

Some discussion is made here of the so-called stable layering of beads observed by Anilkumar (1989) and Anilkumar et al (1993). If the bed is composed of three layers, all of the same diameter, with steel beads in the top one-thirds of the bed with density 7800 kg/m^3 , glass in the middle one-third with density

2500 kg/m³, and polystyrene in the lower one-third with density 1040 kg/m³, then Anilkumar observes cracks forming initially, then closing up during subsequent upward movement. The variation in bead density with depth affects the cohesion S_{0c} by making it piecewise linear as illustrated in Fig. (11). There will be other effects of layering on cohesion that are not known and not modelled here, for example due to different electrostatic forces on polystyrene beads compared to steel beads.

The reduction process leading to a linear gas diffusion problem combined with the strain equation is not affected by the relatively small changes in density. The solution p of the gas diffusion problem is the same as for a uniform bed of beads, since bead sizes are all the same. The gravity term 1 in the boundary-value problem (35) will change to a scaled density that is piecewise constant and of order one. Hence the shape of w_z will remain the same as before, small for z away from one and with a unique maximum near the place where p is changing appreciably. The rupture criterion is slightly altered as reflected in Fig. (11), and a layer is still predicted to rupture away from the bed due to stress exceeding cohesion there.

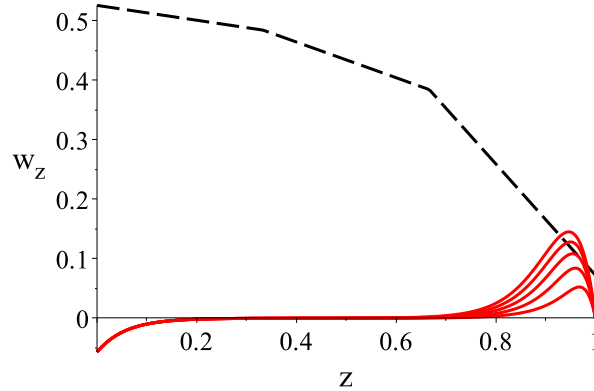


Fig. 11. Rupture condition for a three-layer bed with high density steel beads in the uppermost layer, glass in the middle layer, and lowest density polystyrene in the bottom layer. The dashed line shows the resulting cohesion S_{0c} , to be exceeded by w_z (solid lines, at evenly spaced dimensionless times from zero to $t = 25 \times 10^{-4}$), for bed rupture to occur. The strain w_z is computed by solving the Greens function integration for $w_z z - \lambda_f w = \rho_b - p_z$, where ρ_b is a normalised bead density, taking the value 0.4 for $z < 1/3$, 1.0 for $1/3 \leq z < 2/3$, and 3.1 for $z > 2/3$.

When three layers of different sized glass beads are placed in the bed, with the largest beads on top and the smallest beads at the bottom, similar behaviour is observed by Anilkumar (1989) and Anilkumar et al (1993) — multiple cracks form initially, then close up during subsequent upward movement. Modelling this situa-

tion with our approach gives the same cohesion as illustrated in Fig. (5), since bed density and porosity are the same everywhere. Permeability is the most important parameter to change with particle size, so that the gas diffusion problem becomes one with varying permeability with depth. However, once again the general nature of the resulting solution will be a pressure p that increases monotonically with height. The arguments presented in subsection (4.2) about the shape of w_z apply, so that the general appearance of the rupture condition is similar to that illustrated in Fig. (5).

7. Conclusions

We have explained why layers form when a bed of dust is subjected to shock-tube experiments, by developing, reducing, and solving a mathematical model for the conservation of mass and momentum for adiabatic compressible flow of gas through a porous medium of low cohesion, where the effect of gravity through overburden is taken to be important in the scalings used. The effects of wall friction and the nature of the cohesion of the bed have also been modelled.

The mathematical model reduces to two equations, a linear diffusion equation for pressure changes, which has been solved by elementary techniques, and a linear boundary-value problem for the steady-state solid displacement w , which can be solved once gas pressure is known. If wall friction is ignored, stress can be solved for analytically; otherwise a Green's function solution is provided that can be solved by numerical quadrature. General arguments for a unique local maximum in strain w_z given the typical shape of a pressure diffusion problem have been made. This gives solid stress in the bed, and determines when and where cohesion is overcome.

Pressure drops at the surface of the bed when the expansion fan from the shock chamber reaches it. This drop diffuses into the bed, and lifts a layer off when the effective solid stress exceeds bed cohesion at some depth into the bed. In the absence of wall friction, this can be interpreted in terms of an increasing pressure difference that penetrates deeper into the bed as it grows, and eventually matches overburden plus cohesion at some depth, whereupon a layer of dust ruptures and lifts off. This process is then set to repeat again and again, rupturing the dust bed in regular layers.

The least well-determined parameter in the model is the cohesion, and this parameter was adjusted within a reasonable range, to obtain a good match to experimental results.

Once a single layer lifts off, previous work (Fowler et al., 2009; McGuinness et al., 2012) shows that to a good approximation the pressure at the surface of the remaining stationary bed might be anticipated to follow p_c , so that the analysis giving the rupture of one layer applies again and again, giving multiple layers in succession, all of similar size since the only parameter that is changing is the length l of the remaining bed.

The dependence of layer size on bead diameter is explored using a small time small $1 - z$ approximation that gives a good match to experimental values, and to numerical experiments using a more accurate pressure solution. In contrast to Anilkumar’s speculation that layer size varies as the square root of bead diameter (Anilkumar, 1989), we find a theoretical basis for layer size to be proportional to bead diameter, in the range of diameters considered, which is a good fit to Anilkumar’s results. Further experimentation with larger and smaller bead diameters and different over-pressures would be useful to verify our layer size predictions.

Our modelling results are consistent with reported observations of layered beds, with heavier beads above or below lighter beads, or with larger beads above or below smaller beads, in that bed rupture is always predicted to occur for large enough values of p_0 . Subsequent repacking, where in some (stable) bed configurations the layers move closer and close up the gaps between, is then due to the kinematics of the relative layer speeds. Larger diameter dusts are predicted here to fragment in larger slabs, which will accelerate more slowly than the smaller slabs of smaller diameter dusts. This is consistent with experimental observations (Anilkumar, 1989) that larger diameter dusts overlying smaller is a stable configuration, that is, slabs do not persist after mobilisation. A similar explanation applies to the stable configuration of denser material like steel spheres overlying low density material like glass of the same diameter — slab size is predicted to be the same in both materials, with the same pressure differences driving ejection, but the denser material leads to denser slabs which will accelerate more slowly.

Cohesion is also critically dependent on moisture content and static electricity charges. The theory presented here provides a framework for theoretical investigations into the dependence of layer formation on moisture content, provided that theoretical development of the effect of moisture on cohesion is made, which would be very interesting to support and verify with further experimental work.

The implications for Vulcanian and Plinian eruptions of the mathematical modelling results found here, in combination with the work done previously on fragmentation of competent rock samples (Fowler et al., 2009; McGuinness et al., 2012), are that fragmentation is always initiated in an inhomogeneous manner, producing slabs or layers with a characteristic length scale, irrespective of

whether the material being mobilised is competent volcanic rock or a powder with very small cohesivity. These slabs are then propelled upwards by pressure differences. The experiments of Anilkumar (1989) show that in the special case that heavier powder material overlies lighter material, or larger diameter dusts overly smaller, the initial gaps between slabs of powder may be closed up by kinematic processes. These results then have various implications for the behaviour of the source material for ejected volcanic plumes, suggesting as a general principle that source inhomogeneity rather than homogeneity is to be expected.

Acknowledgments

We are grateful to Professor Andrew Fowler (Math. Inst., University of Oxford and MACSI, University of Limerick) for fruitful discussions that helped us to progress this work, to Professor Colin Wilson at Victoria University of Wellington for the comments that started our interest in erupting dusts, and to Professor Amrutur V. Anilkumar (Department of Mechanical Engineering, Vanderbilt University) for his comments and for permission to use his erupting dust figures. Mark McGuinness acknowledges financial support from Science Foundation Ireland Grant SFI/12/IA/1683.

Appendix A. Cohesion

We present here a brief summary of the tensile strength of granular materials, that is focussed on finding a reasonable range of possible values for the cohesion of the glass beads under consideration, with diameters of 125, 500 and 750 μm .

In seminal work summarised by Molerus (2002), the adhesion force at a contact for an unconsolidated or uncompressed glass powder bulk is (see also Molerus (1993))

$$H_0 \approx 9 \times 10^{-8} \text{ N}$$

and the number of contacts $N_k(\phi)$ is approximately six for each bead. The tensile strength of the bulk powder in the absence of any history of compression is then given by

$$\sigma_0 = \frac{(1 - \phi)N_k(\phi)}{\pi D_p^2} H_0 \approx \frac{10^{-7}}{D_p^2} \text{ Pa} . \quad (\text{A.1})$$

Resulting values for the diameters we consider here are

$$\sigma_0 = 40 \text{ Pa for } D_p = 50 \mu\text{m} , \quad (\text{A.2})$$

$$\sigma_0 = 7 \text{ Pa for } D_p = 125 \mu\text{m} , \quad (\text{A.3})$$

$$\sigma_0 = 0.4 \text{ Pa for } D_p = 500 \mu\text{m} , \quad (\text{A.4})$$

$$\sigma_0 = 0.2 \text{ Pa for } D_p = 750 \mu\text{m} . \quad (\text{A.5})$$

Note that at a diameter of about $200\mu\text{m}$ this becomes of the same order as the gravitational pressure 1Pa due to one diameter of overburden.

For larger beads, there is evidence that the cohesion changes to become of the order of the gravitational pressure associated with one diameter of over-burden (Weir, 1999). This effective geometric cohesion is independent of the internal angle of friction, and is found (Weir, 1999) to give a match between the exact solution to the rigid-plastic flow equations and an extended Beverloo equation based on empirical observations of granular flow. It takes the value $\sigma^0 = (1-\phi)\rho_s g D_p / 2$. It captures the purely geometric effect of a bead being in contact with its neighbours and the receptacle walls. The parameters σ_0 and σ^0 become of similar size when $D_p \approx 200 \mu$. We take the effective cohesion of an unconsolidated bed to be

$$S_0 = \sigma_0 + \sigma^0 .$$

Consolidation

Molerus (2002) notes that previous consolidation by a compressive force N_0 can change the contact surface area between beads due to plastic behaviour, and leads to the increased cohesive force

$$H = H_0 + \kappa N_0 ,$$

and the cohesion of a previously consolidated bed is then $S_{0c} = S_0 + \kappa \sigma_{N0} = \sigma_{0c} + \sigma^0$, where

$$\sigma_{0c} = \frac{(1-\phi)N_k(\phi)}{\pi D_p^2} H = \sigma_0 + \kappa \sigma_{N0} \text{ Pa} . \quad (\text{A.6})$$

Experimental results (Molerus, 1993, 2002) suggest that cohesion is very sensitive to prior compression forces, and experimental values $\kappa \approx 0.3$ are also a good match to theoretical values, for N_0 values up to similar order to H_0 values.

Two possible sources of compression in the shock-tube experiments are the manner in which the bed is charged with high pressure gas σ_{NC0} , and the gravity effect of overburden of material in the bed σ_{NG0} , so that

$$\sigma_{N0} = \sigma_{NC0} + \sigma_{NG0} .$$

Charging with nitrogen during the setup of the experiment could lead to the bed being compressed, depending on the rate of charging. Anilkumar's test setup is charged from a high-pressure cylinder of nitrogen to a port above the top of the bed, controlled by a solenoid valve.

A simple two-chamber pressure model allows us to estimate the compression effect on the bed, of charging the chamber. Consider the average pressure p_1 in the chamber of volume V_1 above the bed, and containing a mass M_1 of gas, being charged at a mass rate R_1 (kg/s), and bleeding at a mass rate $R_2(p_1 - p_2)$ (kg/s) into the second chamber which is the bed itself with an average bed pressure p_2 , total pore volume V_2 , and containing a mass M_2 of gas. Conservation of gas mass gives

$$\begin{aligned}\frac{dM_1}{dt} &= R_1 - R_2(p_1 - p_2) , \\ \frac{dM_2}{dt} &= R_2(p_1 - p_2) ,\end{aligned}$$

Taking isothermal conditions for simplicity, together with the ideal gas law, gives the pressure equations

$$\begin{aligned}\frac{dp_1}{dt} &= C_1 - C_2(p_1 - p_2) , \\ \frac{dp_2}{dt} &= C_3(p_1 - p_2) ,\end{aligned}$$

where $C_1 = R_1RT/(V_1M)$, $C_2 = R_2C_1/R_1$, and $C_3 = C_2V_1/V_2$, R is the gas constant, T is temperature, and M is the molar mass of the gas.

Subtracting the second equation from the first, and taking both pressures to start from atmospheric pressure, gives the following differential equation for the pressure difference $\Delta p = p_1 - p_2$:

$$\frac{d}{dt}(\Delta p) = C_1 - (C_2 + C_3)\Delta p$$

with initial condition $\Delta p = 0$. Assuming for simplicity a controlled constant pressure charge rate C_1 (Pa/s), and constant R_2 , the solution is

$$\Delta p = \frac{C_1}{C_2 + C_3} \left(1 - e^{-(C_2 + C_3)t}\right) ,$$

which starts at zero and rises towards the asymptotic value $C_1/(C_2 + C_3)$. The pressure difference decays only after charging is turned off.

This asymptotic value for Δp is used as a proxy for the compression imposed on the bed by charging with nitrogen. We now estimate values for C_1 and $C_2 + C_3$ to provide a value for this compression.

Discharge from a typical bed setup takes about 40 ms in Anilkumar's experiments, so taking a timescale of 40ms to charge the bed with a given pressure difference imposed suddenly above the bed, gives $C_2 + C_3 \approx 50\text{s}^{-1}$.

If the charge valve is opened gradually over a time of two minutes for a total charge of 200 kPa, the charging rate is approximated by $C_1 = 1660\text{ Pa/s}$.

The compressive pressure on the bed associated with charging is then estimated at $\sigma_{NC0} = C_1/(C_2 + C_3) \approx 33\text{Pa}$. For beads bigger than $50\text{ }\mu\text{m}$ the cohesion σ_{0c} is then significantly altered from σ_0 . If the charge valve is opened over a period of two seconds rather than two minutes, the same calculation leads to the value $\sigma_{NC0} \approx 2000\text{Pa}$. There is clearly a large degree of variability in this value, depending on experimental conditions and setup, with our calculations suggesting that a reasonable range of values for σ_{NC0} is 30–2000 Pa.

The second possible source of compression is the overburden in the bed. The pressure due to solid overburden at dimensionless height z , is

$$\sigma_{NG0} = (1 - \phi)\rho_s g l(1 - z) .$$

This ranges in value from zero to about 670 Pa, from top to bottom of the bed.

Note that here we are not modelling the effect of overburden on momentum conservation or a force balance, as this is already done above. We are considering the effect of the compression associated with overburden on the contact area between beads, and hence on bed cohesion. A similar calculation is made by Orband & Geldart (1997) to explain cohesions observed in measurements made on $64\text{ }\mu\text{m}$ glass ballotini that are six times larger than the unconsolidated values.

The compression term is approximated for the shock tube experiments as

$$\kappa\sigma_{N0} = \kappa\sigma_{NC0} + \kappa(1 - \phi)\rho_s g l(1 - z) \approx (9 - 600) + 670(1 - z) \text{ Pa} . \quad (\text{A.7})$$

The effects of prior compaction by vibration of the bed can be significant for smaller sized beads, according to a recent study by Xu & Zhu (2006), where tensile strength measured by the overshoot pressure at incipient bed fluidisation varies by factors of up to four as prior compaction varies.

A Warren Spring-Bradford apparatus is used by Orband & Geldart (1997) to measure the cohesion of freely-flowing powder samples with mean sizes from 20 to $120\text{ }\mu\text{m}$. They find a range of values, all greater than 100Pa, with almost

constant apparent cohesion above a critical size. For glass ballotini at $67 \mu\text{m}$ diameter they measure a tensile strength of 140Pa.

A number of other factors can affect the apparent cohesion of a powder, including the amount of moisture present, vibration (Xu & Zhu, 2006), and electrostatic forces. Emery et al (2009) discuss the various possible effects of moisture on tensile strength, ranging from liquid bridging across particle contacts to decreased electrostatic forces. Mikami et al (1998) develop numerical simulations of the effects of moisture on tensile strength in a fluidised bed, and also discuss the modelling of wall friction. Weber (2004) explores the importance of liquid bridging forces, in a study of the pressure overshoot and hysteresis often seen at incipient fluidisation in plots of pressure difference across a bed versus steady fluid velocity. He finds that particle-particle cohesion dominates wall friction and cohesion with the bottom of the bed container, although the latter do have some effect on the overshoot.

However, it is unclear what steps were taken to dry the beads used in Anilkumar's experiments, and what the charging method was. Anilkumar notes in a private communication that charging of the bed was slow, taking several minutes to complete, that the glass particles were free-flowing, and that there were no moisture-related issues.

To summarise, the criterion for bed rupture is given in terms of the effective cohesion of a possibly consolidated bed as

$$(1 - \phi)(\sigma + p) > S_{0c} \quad (\text{A.8})$$

where

$$S_{0c} = \sigma_{0c} + \sigma^0 = \sigma_0 + \kappa\sigma_{N0} + \sigma^0 \quad (\text{A.9})$$

where σ_0 is given by eqn (A.1), $\kappa\sigma_{N0}$ is given by eqn (A.7), and

$$\sigma^0 = (1 - \phi)\rho_s g D_p / 2 .$$

References

- Abramowitz, M., & Stegun, I., 1972. Handbook of Mathematical Functions. Dover, NY.
- Alidibirov, M., 1994. A model for viscous magma fragmentation during volcanic blasts. Bulletin of Volcanology 56, 459–465.

- Anilkumar, A.V., 1989. Experimental studies of high-speed dense dusty gases. Ph.D. Thesis, Aeronautics, California Institute of Technology, Pasadena, CA, USA.
- Anilkumar, A.V., Sparks, R.S.J., Sturtevant, B., 1993. Geological implications and applications of high-velocity two-phase flow experiments, *J. Volcanol. Geoth. Res.*, 56, 145–160.
- Biot, M.A., 1956. Theory of propagation of elastic waves in a fluid-saturated porous solid. I. Low-frequency range. *J. Acoust. Soc. Amer.* 28, 168–178.
- Biot, M.A., 1962. Mechanics of deformation and acoustic propagation in porous media. *J. Appl. Phys.* 33, 1,482–1,498.
- Cagnoli, B., Barmin, A., Melnik, O., Sparks, R.S.J., 2002. Depressurization of fine powders in a shock tube and dynamics of fragmented magma in volcanic conduits *Earth & Planetary Sci. Lett.* 204, 101–113.
- Cashman, K.V., Sturtevant, B., Papale, P., Navon, O., 2000. Magmatic fragmentation. In: *Encyclopedia of Volcanoes*, Ed. Sigurdsson, H., Academic Press, SanDiego, 421–430.
- Coelho, D., Thovert, J.-F., and Adler, P.M., 1997. Geometrical and transport properties of random packings of spheres and aspherical particles *Phys. Rev. E*, v. 55, No. 2, 1959–1978.
- Costa, A., 2006. Permeability-porosity relationship: A re-examination of the Kozeny-Carman equation based on a fractal pore-space geometry assumption. *Geophys. Res. Lett.* 33: L02318. doi:10.1029/2005GL025134
- Crank, J., 1975. *The Mathematics of Diffusion*, 2nd Edn, Clarendon Press, Oxford.
- Dartevell, S., and Valentine, G.A. (2007), Transient multiphase processes during the explosive eruption of basalt through a geothermal borehole (Nmafjall, Iceland, 1977) and implications for natural volcanic flows. *Earth and Planetary Sci. Lett.* 262, 363–384.
- Dingwell, D. B. & Webb, S. L., 1989. Structural relaxations in silicate melts and non-newtonian melt rheology in geologic processes. *Phys. Chem. Miner.* 16, 508–516. (doi:10.1007/BF00197020)

- Emery, E., Oliver, J., Pugsley, T., Sharma, J., & Zhou, J., 2009. Flowability of moist pharmaceutical powders. *Powder Tech.* 189, 409–415.
- Ergun, S., 1952. *Chem. Eng. Prog.*, 48, 89p.
- Fowler, A.C., Scheu, B., Lee, W.T., McGuinness, M.J., 2009. A theoretical model of the explosive fragmentation of vesicular magma. *Proc. Roy. Soc. Lond., A*, March 8, 2010, 466:731–752; published online before print November 3, 2009. doi:10.1098/rspa.2009.0382
- Geldart, D., 1973. *Powder Technol.*, 7, 285.
- Gilbert, J.S., Sparks, R.S.T. (eds), 1998. The physics of explosive volcanic eruptions. Geological Soc. Special Publications No. 145, London, UK: Geological Society.
- Heiken G., Wohletz, K., 1991. Fragmentation processes in explosive volcanic eruptions. In: *Sedimentation in volcanic settings*, Society for Sedimentary Geology, Special Publications No. 45, 19–26.
- Ichihara, M., Rittel, D., Sturtevant, B., 2002. Fragmentation of a porous viscoelastic material: implications to magma fragmentation. *J. Geophys. Res.* 107 (B10), 2229. doi:10.1029/2001JB000591
- Jaraiz, E., Kimura, S., Levenspiel, O., 1992. Vibrating beds of fine particles: estimation of interparticle forces from expansion and pressure drop experiments. *Powder Tech.* 72, 23–30.
- Kameda, M., Kuribara, H., Ichihara, M., 2008. Dominant time scale for brittle fragmentation of vesicular magma by decompression. *Geophys. Res. Lett.* 35, L14302. doi:10.1029/2008GL034530
- Mader, H.M., Zhang, Y., Phillips, J.C., Sparks, R.S.J., Sturtevant, B., Stolper, E., 1994. Experimental simulations of explosive degassing of magma. *Nature* 372, 85–88.
- Mangan, M.T., Cashman, K.V., 1996. The structure of basaltic scoria and reticulite and inferences for vesiculation, foam formation, and fragmentation in lava fountains. *J. Volcanol. Geoth. Res.*, 73, 1–18.

- Martel, C., Dingwell, D.B., Spieler, O., Pichavant, M., Wilke, M., 2000. Fragmentation of foamed silicic melts: an experimental study. *Earth and Planetary Science Letters* 178, 47–58.
- McBirney, A.R., Murase, T., 1970. Factors governing the formation of pyroclastic rocks. *Bull. Volc.* 34, 372–384.
- McGuinness, M.J., Scheu, B., Fowler, A.C., 2012. Explosive fragmentation criteria and velocities for vesicular magma, *J. Volc. and Geothermal Res.*, 237–238, 81–96. <http://dx.doi.org/10.1016/j.jvolgeores.2012.05.019> or <http://www.sciencedirect.com/science/article/pii/S0377027312001576>
- Melnik, O., 2000. Dynamics of two-phase conduit flow of high-viscosity gas-saturated magma: large variations of sustained explosive eruption intensity. *Bull. Volcanol.* 62, 153–170. (doi:10.1007/s004450000072)
- Mikami, T., Kamiya, H., & Horio, M., 1998. Numerical simulation of cohesive powder behaviour in a fluidised bed. *Chem. Eng. Science* 53, No. 10, 1927–1940.
- Molerus, O., 2002. The role of science in particle technology. *Powder Tech.* 122, 156–167.
- Molerus, O., 1993. *Principles of Flow in Disperse Systems*. Chapman & Hall, London, 1993.
- Namiki, A., Manga, M., 2005. Response of a bubble bearing viscoelastic fluid to rapid decompression: implications for explosive volcanic eruptions. *Earth and Planetary Science Letters* 236, 269–284.
- Orband, J.L.R. & Geldart, D., 1997. Direct measurement of powder cohesion using a torsional device. *Powder Tech.* 25–33.
- Papale, P., Neri, A. & Macedonio, G., 1998. The role of magma composition and water content in explosive eruptions. I. Conduit ascent dynamics. *J. Volcanol. Geotherm. Res.* 87, 75–93. (doi:10.1016/S0377-0273(98)00101-2)
- Papale, P. 1999. Strain-induced magma fragmentation in explosive eruptions. *Nature* **397**, 425–428.

- Phillips, J.C., Lane, S.J., Lejeune, A.M., & Hilton, M., 1995. Gum rosin-acetone system as an analogue to the degassing behaviour of hydrated magmas. *Bulletin of Volcanology* 57, 263–268.
- Scheu, B., Spieler, O., Dingwell, D.B., 2006. Dynamics of explosive volcanism at Unzen volcano: an experimental contribution. *Bulletin of Volcanology* 69 (2), 175–187.
- Scheu, B., Ichihara, M., Spieler, O., Dingwell, D.B., 2008. A closer look at magmatic fragmentation. *Geophys. Res. Abst.* 10, EGU2008-A-04786.
- Sparks, R.S.J., 1978. The dynamics of bubble formation and growth in magmas: a review and analysis. *J. Volc. Geoth. Res.* 3, 1–37.
- Spieler, O., Kennedy, B., Kueppers, U., Dingwell, D.B., Scheu, B., Taddeucci, J., 2004b. The fragmentation threshold of pyroclastic rocks. *Earth and Planetary Science Letters* 226, 139–148.
- Tanneur, V., Jousset-Dubien, C., Fournel, B., Sarrade, S., Freiss, B., Marciacq, F., & Rios, G.M., 2008. Group A particle fluidization in supercritical carbon dioxide: Effect of operating conditions on fluidization efficiency. *Powder Tech.* 187, 190–194.
- Valverde, J.M., Ramos, A., Castellanos, A., & Watson, P.K., 1998. The tensile strength of cohesive powders and its relationship to consolidation, free volume and cohesivity. *Powder Tech.* 97, 237–245.
- Verhoogen, J., 1951. Mechanics of ash formation. *Am. J. Sci.* 249, 729–739.
- Weber, M.W., 2004. Simulation of cohesive particle flows in granular and gas-solid systems, a thesis submitted for the degree of Doctor of Philosophy, Dept. of Chemical and Biological Eng., University of Colorado.
- Weir, G.J., 1999. The intrinsic cohesion of granular materials. *Powder Tech.* 104, 29–36.
- Xu, C., & Zhu, J., 2006. Parametric study of fine particle fluidization under mechanical vibration. *Powder Tech.* 161, 135–144.